

# Manipulating Fock states of a harmonic oscillator while preserving its linearity

K. Juliusson<sup>1</sup>, S. Bernon<sup>1</sup>, X. Zhou<sup>1</sup>, V. Schmitt<sup>1</sup>, H. le Sueur<sup>2</sup>,  
P. Bertet<sup>1</sup>, D. Vion<sup>1</sup>, M. Mirahimi<sup>3</sup>, P. Rouchon<sup>4</sup>, and D. Esteve<sup>1</sup>

<sup>1</sup>*Quantronics group, SPEC, CEA, CNRS, Université Paris-Saclay, CEA Saclay, 91191 Gif-sur-Yvette, France.*

<sup>2</sup>*Centre de Sciences Nucléaires et de Sciences de la Matière, 91405 Orsay, France.*

<sup>3</sup>*INRIA Paris-Rocquencourt, Domaine de Voluceau,  
B.P. 105, 78153 Le Chesnay Cedex, France. and*

<sup>4</sup>*Centre Automatique et Systèmes, Mines-ParisTech,  
PSL Research University, 60, bd Saint-Michel, 75006 Paris, France.*

(Dated: July 19, 2016)

We present a new scheme for controlling the quantum state of a harmonic oscillator by coupling it to an anharmonic multilevel system (MLS) with first to second excited state transition frequency on-resonance with the oscillator. In this scheme that we call ‘ef-resonant’, the spurious oscillator Kerr non-linearity inherited from the MLS is very small, while its Fock states can still be selectively addressed via an MLS transition at a frequency that depends on the number of photons. We implement this concept in a circuit-QED setup with a microwave 3D cavity (the oscillator, with frequency 6.4 GHz and quality factor  $Q_O = 2 \times 10^6$ ) embedding a frequency tunable transmon qubit (the MLS). We characterize the system spectroscopically and demonstrate selective addressing of Fock states and a Kerr non-linearity below 350 Hz. At times much longer than the transmon coherence times, a non-linear cavity response with driving power is also observed and explained.

The harmonic oscillator being an exactly solvable system with a single degree of freedom, is often taken as a model system in many areas of physics. In particular, for demonstrating coherent control of simple quantum systems, physicists have used cold electromagnetic resonators in the quantum regime, with their quantum states controlled by a single atom, be it a real one in cavity-QED [1] or an artificial one in circuit-QED [2, 3]. For instance, the preparation of a single photon Fock state by passing an atom through a cavity [4], or of an arbitrary quantum state using the Law and Eberly protocol [5–7] in circuit-QED, are landmark results. In circuit-QED relevant to this work, the resonator has a frequency  $\nu_O$  in the microwave domain, and the artificial atom is a superconducting quantum bit that can be regarded as an ancillary multilevel system (MLS) with states  $|g\rangle, |e\rangle, |f\rangle, |h\rangle \dots$  possibly tunable in energy. The MLS can be used resonantly [6, 7], or off-resonantly [8] when its coupling to the resonator is sufficiently strong to split the transition frequency  $\nu_{ge}$  into different lines at frequencies  $\nu_n$  that depend on the photon number  $n$  [9]. In this so-called ‘‘photon number split’’ regime, any particular Fock state  $|n\rangle$  is addressed at frequency  $\nu_n$ , and symmetrically, the resonator can be driven coherently at a frequency  $\nu_{O,|x\rangle}$  that depends on the MLS state  $|x\rangle$ . This allows for both manipulating and measuring the oscillator field in various ways, for instance by MLS-state conditional cavity phase shift [10], photon-number selective phase gates [11] that could lead to universal control of the oscillator field [12], or by Wigner and quantum state tomography of the field [13, 14].

This off-resonant method has been demonstrated with transmon qubits [15] coupled dispersively to the resonator, i.e. with detunings  $|\Delta_{xy} = \nu_{xy} - \nu_O|$  between any  $\nu_{xy}$  transition of the transmon and  $\nu_O$  much larger than the coupling frequency  $g_{xy}$  between this transition

and the cavity field. In this dispersive regime, the frequencies  $\nu_n = \nu_{ge} + n\chi$  are equidistant and separated by the so-called dispersive shift  $\chi \simeq 2\alpha\varepsilon^2$  [15], with  $\alpha = \nu_{ef} - \nu_{ge}$  the transmon anharmonicity,  $\varepsilon = g_O/\Delta$ ,  $g_O \equiv g_{ge}$  the transmon-oscillator coupling, and  $\Delta = \nu_{ge} - \nu_O$  their detuning. A drawback of this scheme is to transfer part of the transmon MLS anharmonicity to the oscillator [16, 17], which can drastically perturb its coherent dynamics [14, 18, 19] and necessitate careful design [16] and correction protocols [11]. This non-linearity [14, 15, 17] results in a shift of the oscillator frequency  $\nu_O$  (or Kerr non-linearity) of about  $K = \alpha\varepsilon^4$  per photon.  $K$  scaling as  $\chi^2/\alpha$  cannot be minimized (at fixed  $\alpha$ ) without losing the selectivity between Fock states. In this work, we propose a different transmon-oscillator coupling scheme (see Fig.1) that yields a much smaller Kerr non-linearity for the same Fock state selectivity. The idea consists in having the  $ef$  transition resonant with  $\nu_O$ , i.e.  $\Delta = -\alpha$ , to displace significantly the qubit excited levels even at small coupling  $g_O$ , while at the same time staying in the dispersive regime for the first transition  $\nu_{ge}$  to get a small non-linearity. We explain in details in the next section this ‘ef-resonant’ condition when the MLS is a slightly anharmonic three level system, for which analytic results can be obtained. Then, we describe in section II our implementation of the proposal, and characterize it experimentally in section III.

## I. THE ‘EF-RESONANT’ COUPLING SCHEME FOR A HARMONIC OSCILLATOR

To explain the interest of our coupling scheme in the simplest way, we first consider the case of a harmonic oscillator ( $O$ ) with frequency  $\nu_O$  and annihilation operator  $a$ , coupled to a three-level system (3LS) with eigenstates

$\{|g\rangle, |e\rangle, |f\rangle\}$  and lowering operator  $a_q$ . We also assume a weak anharmonicity  $\alpha = \nu_{ef} - \nu_{ge} \ll \nu_{ge}$ , such that  $a_q$  can be approximated by the annihilation operator of a harmonic oscillator restricted to three levels. The two subsystems obey the resonant condition  $\nu_{ef} = \nu_O$  (detuning  $\Delta = \nu_{ge} - \nu_O = -\alpha$ ) and are subject to an exchange interaction with coupling frequency  $g_O \ll \alpha$ , yielding the

Hamiltonian

$$\begin{aligned} H &= H_O + H_{3LS} + H_{coupling}, \\ H_O &= h\nu_O a^\dagger a, \\ H_{3LS} &= h(\nu_O a_q^\dagger a_q - \alpha |e\rangle \langle e| - \alpha |f\rangle \langle f|), \\ H_{coupling} &= hg_O (a^\dagger a_q + a a_q^\dagger). \end{aligned} \quad (1)$$

This coupling makes the Hamiltonian matrix block-diagonal in the basis  $|xn\rangle \equiv |x\rangle \otimes |n\rangle$  ( $x = g, e, f$ ), with subsequent blocks of size 1, 2, 3, 3, 3... Using the reduced coupling  $\varepsilon = -g_O/\alpha$ , these blocks write

$$[0]_{|g0\rangle}, h \left( \nu_O I_2 - \alpha \begin{bmatrix} 0 & \varepsilon \\ \varepsilon & 1 \end{bmatrix} \right)_{|g1\rangle, |e0\rangle}, h \left( n\nu_O I_3 - \alpha \begin{bmatrix} 0 & \sqrt{n}\varepsilon & 0 \\ \sqrt{n}\varepsilon & 1 & \sqrt{2(n-1)}\varepsilon \\ 0 & \sqrt{2(n-1)}\varepsilon & 1 \end{bmatrix} \right)_{B_n}, \quad (2)$$

with  $I_k$  the identity matrix of dimension  $k$  and  $B_n = \{|gn\rangle, |e(n-1)\rangle, |f(n-2)\rangle\}$  the basis for  $n \geq 2$ . The diagonalization of each block yields analytical eigenenergies and vectors, which for  $n \geq 2$  are functions of the three real solutions of the cubic equation  $x^3 - 2x^2 + [1 + 2\varepsilon^2 - 3n\varepsilon^2]x + n\varepsilon^2 = 0$ . To shed light on the

physics, we expand these analytical quantities in the small parameter  $\varepsilon$ . As shown in Fig. 1, the levels form three distinct energy ladders  $\{|\widetilde{gn}\rangle\}$ ,  $\{|-n\rangle\}$  and  $\{|+n\rangle\}$ : The ladder  $\{|\widetilde{gn}\rangle\}_{n>0}$  corresponds to the almost unperturbed oscillator when the 3LS is left in its ground state. With eigenenergies and eigenvectors

$$\begin{aligned} E(|\widetilde{gn}\rangle) &= nh[\widetilde{\nu}_O + (n-1)K/2] + o(\varepsilon^5) \\ |\widetilde{gn}\rangle &= \left[ 1 - n\varepsilon^2/2, -\sqrt{n}\varepsilon, \sqrt{2n(n-1)}\varepsilon^2 \right]_{B_n} + o(\varepsilon^3), \end{aligned} \quad (3)$$

this effective oscillator  $\widetilde{O}$  has a shifted frequency  $\widetilde{\nu}_O = \nu_O + \alpha(\varepsilon^2 - \varepsilon^4)$ , and a small Kerr non-linearity  $K = 2\alpha\varepsilon^4$  inherited from the 3LS. The two other ladders

$\{|\pm n\rangle\}$  (extended down to  $n=0$  by  $|+0\rangle \equiv |-0\rangle \equiv |\widetilde{g0}\rangle$  and  $|+1\rangle \equiv |-1\rangle \equiv |\widetilde{e0}\rangle$ ) have energies and eigenvectors

$$\begin{aligned} \{E(|\pm n\rangle)\} &= \{0, h[\nu_O - \alpha(1 + \varepsilon^2) + o(\varepsilon^3)], \dots, h[n\nu_O - \alpha(1 \pm \sqrt{2(n-1)}\varepsilon + n\varepsilon^2/2 + o(\varepsilon^3))]\} \\ \{|\pm n\rangle\} &= |g0\rangle, \left[ \begin{array}{c} \varepsilon \\ 1 - \frac{\varepsilon^2}{2} \end{array} \right], \dots, \left[ \begin{array}{c} \varepsilon\sqrt{\frac{n}{2}} \pm \sqrt{\frac{n}{n-1}}\frac{7n-8}{8}\varepsilon^2 \\ \frac{1}{\sqrt{2}} \pm \frac{n}{8\sqrt{n-1}}\varepsilon + \frac{(33n-32)n}{64\sqrt{2}(n-1)}\varepsilon^2 \\ \pm \frac{1}{\sqrt{2}} - \frac{n}{8\sqrt{n-1}}\varepsilon + \frac{n^2}{64\sqrt{2}(n-1)}\varepsilon^2 \end{array} \right]_{B_n} + o(\varepsilon^3). \end{aligned} \quad (4)$$

For  $n \geq 2$  the zeroth-order approximation in  $\varepsilon$  of these eigenvectors are simply the symmetric and anti-symmetric superposition of  $|e(n-1)\rangle$  and  $|f(n-2)\rangle$ . A particular ‘‘Fock state’’  $|\widetilde{gn}\rangle$  of  $\widetilde{O}$  is selectively manipulable by addressing the  $|\widetilde{gn}\rangle \rightarrow |\pm(n+1)\rangle$  transitions to the hybridized oscillator-transmon states, at frequencies  $\nu_{\pm n} = \nu_{ge} \pm \sqrt{2n}g_O + (3n+1)g_O\varepsilon/2 + o(\varepsilon^2)$  (with a Rabi frequency about  $\sqrt{2}$  slower for all  $n > 0$  than for the pure  $|g\rangle \rightarrow |e\rangle$  transition). Note that these frequencies

$\nu_{\pm n}$  do not vary linearly with  $n$  as in the usual dispersive case, but as  $\sqrt{n}$ . Selective addressing of  $|\widetilde{gn}\rangle$  requires the separation  $\Delta\nu_{\pm n} = \nu_{\pm(n+1)} - \nu_{\pm n}$  to be larger than the transition linewidth. A second condition is that the driving strength of the  $\nu_{\pm n}$  transition is low enough to avoid driving off-resonantly the neighboring transitions at  $\nu_{\pm(n+1)}$ .

It is now interesting to compare the Kerr non-linearity  $K = 2\alpha(g_O/\Delta)^4$  obtained here with the value  $K' =$

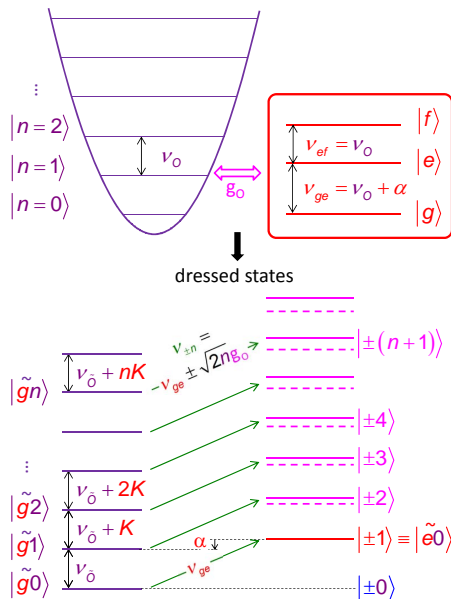


Figure 1. 'MLS ef-resonant' scheme for manipulating Fock states  $|n\rangle$  of a quantum harmonic oscillator. Left: the oscillator with angular frequency  $\nu_O$  is coupled with a coupling frequency  $g_O$  to a multilevel system (MLS) with eigenstates  $\{|g\rangle, |e\rangle, |f\rangle, \dots\}$ , the  $|e\rangle \leftrightarrow |f\rangle$  transition of which is resonant with  $\nu_O$ , whereas the  $|g\rangle \leftrightarrow |e\rangle$  transition is detuned by  $\alpha$ . Right: The resulting energy diagram consists of a quasi-harmonic ladder  $\{|\tilde{g}n\rangle\}$  when the 3LS is left unexcited, and of two anharmonic ladders of levels  $|\pm n\rangle$  that correspond approximately to symmetric and anti-symmetric superpositions of  $|e(n-1)\rangle$  and  $|f(n-2)\rangle$  states for  $n \geq 2$ . The  $|\tilde{g}n\rangle \leftrightarrow |\pm(n+1)\rangle$  transitions can be driven at different frequencies  $\nu_{ge} \pm \sqrt{2(n-1)}g_O$  to manipulate selectively any  $|\tilde{g}n\rangle$ .

$2\Delta' (g'_O/\Delta')^4$  that would be obtained for a two-level system or the value  $K'' = \alpha'' (g''_O/\Delta'')^4$  obtained in perturbation for a transmon in the far dispersive regime  $g''_O, \alpha'' \ll \Delta''$  [17], keeping the same separation  $S = \sqrt{2}g_O = 2\alpha'' (g''_O/\Delta'')^2$  between the first two Fock state dependent excitation frequencies. With respect to the far dispersive case, the new non-linearity is thus reduced by a factor  $K''/K = (\alpha/\alpha'') (\alpha/S)^2/2$  that can be made large easily. This reduction factor, which reaches several hundreds (at fixed transmon anharmonicity  $\alpha = \alpha''$ ) in our implementation of section II, is what makes our 'ef-resonant' scheme interesting. What we show here with a simple ef-resonant 3-LS is that getting out of the perturbation regime  $\alpha'' \ll \Delta''$  reduces drastically the Kerr non-linearity. However considering only three levels makes the argumentation only qualitative for a transmon at large number of photons in the oscillator, and a quantitative evaluation requires taking into account at least the fourth transmon level as we do in section III.

## II. EXPERIMENTAL IMPLEMENTATION

We implement the proposed 'ef-resonant' scheme in a three-dimensional circuit-QED setup [20] combining a cavity with input (1) and output (2) ports and a tunable transmon qubit [15] (see Fig. 2a-b). To be superconducting at low temperature and have a high internal quality factor, the cavity is made of two blocks of pure aluminum, which are milled, pierced, polished, and chemically etched over about 20  $\mu\text{m}$ . The transmon is fabricated on sapphire by double-angle evaporation of Al and oxidation, through a suspended shadow mask made by e-beam lithography. It has two pads connected by a 2.6 mm long wire including a magnetic flux tunable Josephson junction with a SQUID geometry located 50  $\mu\text{m}$  above the bottom pad. This enables tuning the transmon energy spectrum and reaching the 'ef resonant' condition. The transmon is only partly inserted in the cavity so that the SQUID remains about 0.1 mm outside, in the applied external magnetic field. More precisely, the bottom part of the transmon with the SQUID is held and protected by a copper block, the other side being inserted in the cavity through a slit in the bottom wall. The two halves of the cavity are then pressed one against the other with an indium seal in-between.

In our design the TE<sub>120</sub> cavity mode is used as the quantum oscillator  $O$  at frequency  $\nu_O \sim 6.4$  GHz whereas mode TE<sub>210</sub> at frequency  $\nu_R \sim 7.3$  GHz is used for reading the quantum state of the transmon dispersively [2, 3]. The transmon and the ports are thus placed very close to a node of mode  $O$  so that the corresponding coupled quality factor  $Q_O$  is dominated by the internal losses, and the transmon-oscillator coupling  $g_O$  is about 10 MHz. They are also placed at an antinode of mode  $R$  to get a strong transmon-readout coupling  $g_R \sim 150$  MHz and thus a large enough dispersive shift  $\chi_R \sim 10$  MHz, and a low coupled quality factor  $Q_R \sim 15 \times 10^3$  allowing fast readout of the transmon. The exact positions as well as the precise transmon geometry are determined using the CST 3D microwave simulator and methods adapted from [17]. Attention is paid to keep the transmon's charging energy (one electron) below  $300 \text{ MHz} \times h$  in order to avoid variations of the level  $f$  energy due to charge parity fluctuations [21]. For better measurement efficiency, output port 2 is about 6 times more strongly coupled to each mode than input port 1.

The equivalent circuit of the system is shown in Fig. 2c. The transmon-cavity system is mounted inside a coil placed in a mu-metal shield, and is attached to the cold plate of a cryofree dilution refrigerator with base temperature 35 mK. It is connected to the electrical setup of Fig. 2d, which includes a home made quantum limited Josephson parametric amplifier (JPA) similar to [22]. Simple continuous microwave measurements at a single frequency are done with a vectorial network analyzer (VNA), whereas pulsed measurements involving  $\nu_O$ ,  $\nu_R$ , and one or two transmon frequencies use heterodyne modulation and homodyne demodulation as described in

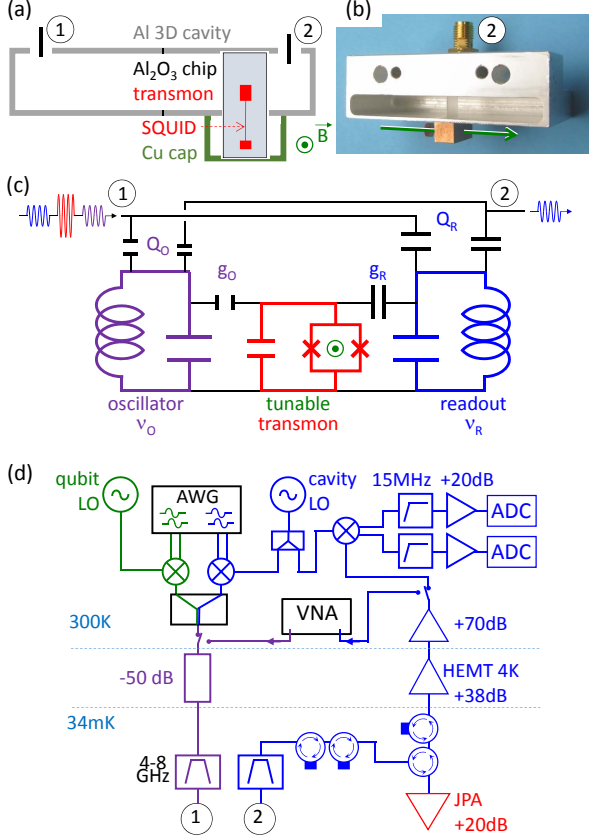


Figure 2. Circuit-QED implementation of the ‘ef-resonant’ scheme. (a) The harmonic oscillator  $O$  is the mode 120 of a superconducting Al cavity and the MLS is a tunable transmon qubit with a SQUID. The transmon chip is inserted only partly in the cavity, the SQUID being exposed to a dc magnetic field  $\vec{B}$ . The transmon is weakly coupled to  $O$  and strongly to the cavity mode 210 used for dispersive readout of the transmon state. The two modes have quality factors  $Q_O = 2 \times 10^6$  and  $Q_R = 15 \times 10^3$ . (b): Picture of one half-cavity with chip and Cu cap. (c) Equivalent electric circuit of the system with relevant frequencies  $f_{R,O}$ , quality factors  $Q_{R,O}$ , and coupling frequencies  $g_{R,O}$ .  $O$  is driven coherently and resonantly through port 1 (purple pulse). Fock state  $|gn\rangle$  are manipulated by driving the  $|\widetilde{gn}\rangle \rightarrow |+n\rangle$  transition (red pulse). A projective measurement on Fock state  $|\widetilde{gn}\rangle$  is obtained by a  $\pi$  pulse at  $\nu_{+n}$  followed by a readout pulse (in blue). (d) Electrical setup at room temperature (300K) and inside the dilution refrigerator: Cavity resonances are measured with continuous waves using a vectorial network analyzer (VNA) whereas pulsed experiments use heterodyne modulation and demodulation. Microwave pulses at the cavity (qubit) frequencies  $\nu_{O,R}$  ( $\nu_{+n}$ ) are obtained by single sideband mixing of a continuous microwave (LO) with an intermediate frequency modulated pulse generated by two channels of an arbitrary waveform generator (AWG). All pulses travel along an attenuated and filtered line to cavity port 1. The readout signal transmitted at port 2 is filtered, isolated from backward propagating noise, amplified with a parametric amplifier (JPA) in reflection, a high electron mobility transistor (HEMT), and room temperature amplifiers, then demodulated to produce two quadratures, which are finally filtered, amplified and digitized (ADC).

Fig. 2d.

### III. EXPERIMENTAL RESULTS

#### A. Spectroscopic characterization

Once at 35 mK, the system is first characterized with the VNA as a function of the current in the coil (see Fig. 3a-b). The lowest transition frequencies of the hybridized readout mode-transmon system yields two peaks at frequencies (red points) that are periodic in flux  $\Phi$ , one period corresponding to one flux quantum  $\Phi_0 = h/2e$ . Away from the avoided crossing, these peaks tend to  $\nu_R$  and  $\nu_{ge}$ . At  $\Phi \simeq 0.5\Phi_0$ , modes  $R$  and  $O$  are unperturbed and one gets their frequencies (central peaks of panels b-top and b-bottom) as well as the total quality factor  $Q_O = 2.2 \times 10^6$  of the oscillator, which corresponds to an energy relaxation time  $T_O = 54 \mu\text{s}$ . At  $\Phi = 0.23\Phi_0$  and  $0.31\Phi_0$  the transmon frequency  $\nu_{ge}$  anti-crosses  $\nu_R$  and  $\nu_O$ , yielding the double peaks of panels b-top and b-bottom, separated by twice the coupling frequencies  $g_R = 149 \text{ MHz}$  and  $g_O = 7.45 \text{ MHz}$ . The setup for pulsed spectroscopy is then used to excite the transmon-oscillator system with one or several pulses, and then detect this excitation from a change of the transmission  $S_{21}(\nu_R)$  of the readout mode (see pulses in Fig. 2c). Figure 3c shows how the readout line is dispersively shifted when the transmon is left in  $|g\rangle$ , partly excited in  $|e\rangle$  with a single pulse at  $\nu_{ge}$ , or partly excited in  $|f\rangle$  with the same first pulse and a second one at  $\nu_{ef}$ . The different readout lines g,e and f do not overlap so that at the top of any peak, a change of the qubit state induces a complete suppression of the transmission. The  $\nu_{ef}(\Phi)$  dependence (green line in panel a) is thus obtained by finding first  $\nu_{ge}(\Phi)$  and then scanning for each  $\Phi$  a second tone around  $\nu_{ef}$  and measuring  $S_{21}(\nu_{R,e})$  at the top of the e readout peak.

The ‘ef-resonant’ condition that we target occurs at  $\Phi_{ef-r} = 0.291\Phi_0$  (vertical cyan line in panel a), when the  $ef$  transition crosses  $\nu_O$ , leading to the hybridization discussed in section I and to the splitting of the  $ef$  peak into two symmetric peaks  $\nu_{e0 \rightarrow \pm 1}$  (shown in magenta in panel b-middle). The dataset of panel b yields the effective anharmonicity  $\alpha = -261 \text{ MHz}$  (‘effective’ means here in presence of the additional readout mode that shifts dispersively the transmon levels). From now on, the system is further characterized at  $\Phi_{ef-r}$  with  $S_{21}(\nu_{R,g})$  being measured at the top of the  $g$  readout peak (see panel c). At this point, we obtain the qubit relaxation time  $T_1 = 1.9 \mu\text{s}$  and coherence time  $T_2^* = 2.4 \mu\text{s}$ . The photon resolved transition frequencies  $\nu_{\pm n}$  are then found by filling mode  $\widetilde{O}$  with a coherent state  $|\beta\rangle = \sum \sqrt{p_\beta(n)} |n\rangle$  using a first resonant excitation pulse at  $\nu_{\widetilde{O}}$  and scanning the frequency of a second pulse about  $\nu_{ge}$ . Panel d shows the peaks at frequencies  $\nu_n$  for  $n = -1, 0, 1, \dots, 16$ , resulting from three different values of  $\beta$ ; the peak amplitudes for each  $\beta$  approximately reproduce the Poisson distribu-

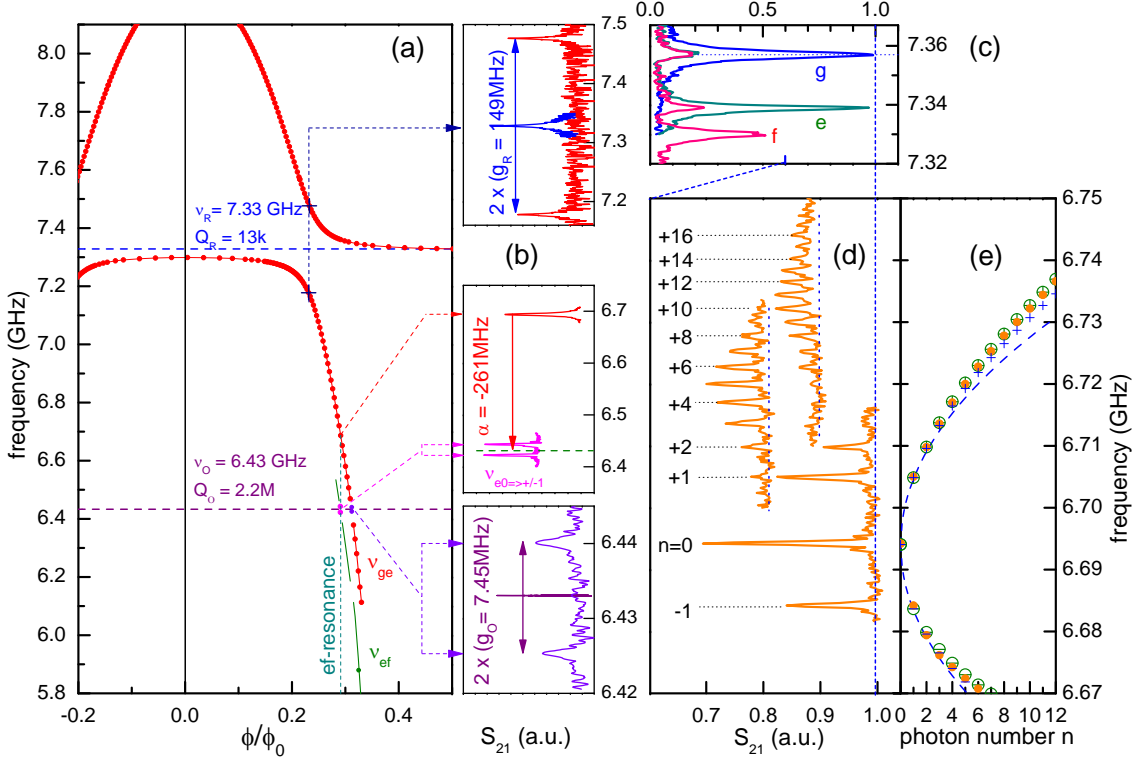


Figure 3. Spectroscopic characterization of the system. (a) Measured transition frequencies as a function of the magnetic flux  $\phi$  applied through the transmon SQUID. Blue and purple horizontal dashed lines correspond to the readout and oscillator frequencies  $\nu_R$  and  $\nu_O$ , red dots to the hybridization of  $\nu_{ge}$  and  $\nu_R$ , and the green line to  $\nu_{ef}$ . The 'ef-resonant' condition is obtained at  $\nu_O = \nu_{ef}$ . (b) Spectra determining the qubit-resonator coupling frequencies  $g_{R,O}$ , as well as the qubit anharmonicity  $\alpha$ . Top: spectra around  $\nu_R$  with  $\nu_{ge}$  either far away (blue peak) or anti-crossing  $\nu_R$  (two red peaks). Bottom: spectra around  $\nu_O$  with  $\nu_{ge}$  either far away (purple peak) or anti-crossing  $\nu_O$  (two violet peaks). Middle: spectrum at the 'ef-resonant' working point showing the  $ge$  (red) and  $|\tilde{e}0\rangle \rightarrow |\pm 1\rangle$  (magenta) transitions. (c) Readout resonance when the qubit is left in  $|g\rangle$  or excited in  $|e\rangle$  or  $|f\rangle$ . Note that the residual thermal population of level  $e$  is well below 1%. The dashed line indicates the frequency at which the readout mode transmission  $S_{21}$  is measured in panel (d). (d) Qubit spectra measured at the 'ef-resonant' point for three different fillings of  $\tilde{O}$  ( $\beta \approx 0.54, 4.5$  and  $10$  - last two horizontally shifted for clarity), showing transitions  $|\tilde{g}n\rangle \leftrightarrow |\pm n\rangle$  (noted  $\pm n$ ) from  $-n = -1$  to  $n = 17$ . (e) Transition frequencies  $\nu_{\pm n}$  deduced (orange dots) from spectroscopy (d), calculated in section I (+ and - symbols), and numerically computed by diagonalization of the system Hamiltonian (open circles). Lines correspond to the parabolic approximation  $\nu_{\pm n} \approx \nu_{ge} \pm \sqrt{2}ng_O$ .

tions  $p_\beta(n)$  expected for coherent states. As opposed to the dispersive case and as expected, the peaks get nearer to each other with increasing  $n$ : in panel e their frequencies (orange dots) are compared to the analytical expression of section I (calculated with three transmon levels) and to the  $\nu_{\pm n}$  values resulting from the numerical diagonalization of an effective oscillator-transmon Hamiltonian also including the fourth transmon level  $h$  (the numerical diagonalization with only three levels coincide with analytical results). A good agreement is found between the experiment and the effective four-level transmon model using the measured values of  $\nu_O$ ,  $\nu_{ge}(\Phi_{ef-r})$ ,  $\alpha$  and  $g_O$ , as well as the shifted energy  $h(3\nu_{ge} - 848 \text{ MHz})$  of eigenstate  $|h\rangle$  calculated from  $\nu_R(\Phi_{ef-r})$  and  $g_R$ .

## B. Oscillator field characterization by selective $\pi$ pulses on $+n$ transitions

Having characterized the system energy diagram, we now address individually the photon number resolved transitions  $+n$  to fully characterize the field and probe the harmonic character of oscillator  $\tilde{O}$ : as an example, we fill  $\tilde{O}$  with coherent states  $|\beta\rangle$  and retrieve them by standard quantum state tomography. This tomography involves the measurement of the occupation probabilities  $p(n)$  of several Fock states  $|n\rangle$ . As done in [14] for the dispersive case, the Fock state population  $p(n)$  is simply transferred to a qubit excited state, which is then read out. In our 'ef-resonant' scheme this transfer between  $|\tilde{g}n\rangle$  and  $|+n\rangle$  consists in applying a  $\pi$  pulse on the  $+n$  transition. These  $\pi$  pulses at frequencies  $\nu_{+n}$  have a Gaussian shape with 140 ns-long standard deviation, and



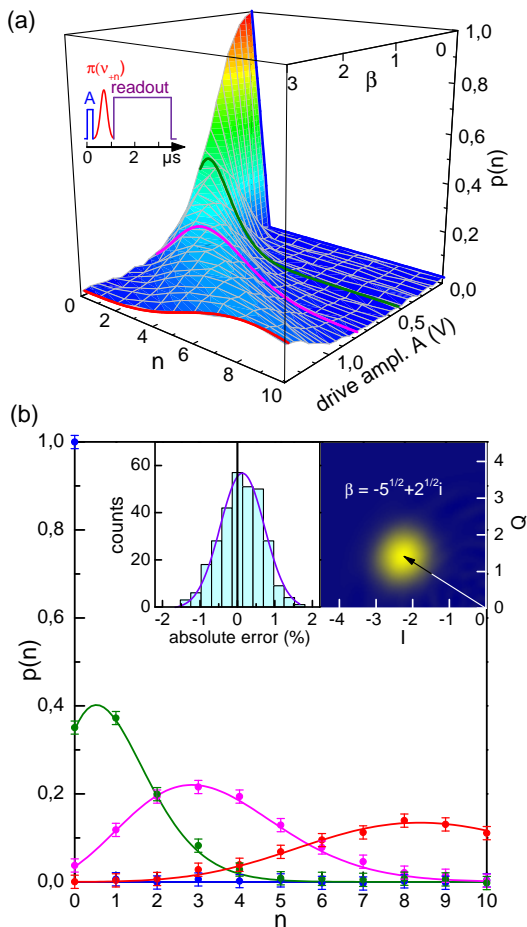


Figure 4. Generation and measurement of coherent states  $|\beta\rangle$  in the oscillator mode: a state is obtained from a  $0.3\ \mu\text{s}$  long rectangular pulse with frequency  $\nu_{\tilde{O}}$  and amplitude  $A$  (expressed here in Volt on the AWG of fig. 2d); a  $\pi$  pulse on one of the  $+n$  transition then excites conditionally the transmon and the variation  $\Delta S_{21}(\nu_R, A, n)$  of the cavity transmission is measured. (a) Occupation probability  $p(n)$  of Fock state  $|n\rangle$  for  $n \in [0, 10]$  and for increasing  $A$ .  $p(n)$  is obtained by dividing  $\Delta S_{21}(\nu_R, A, n)$  by a calibration factor  $c_n$  resulting from a fit of the coherent model  $\beta(A) = kA$  to the whole dataset: the fitted coefficients  $\{c_0, \dots, c_{10}\} = \{0.764, 0.835, 0.847, 0.846, 0.833, 0.854, 0.846, 0.834, 0.847, 0.832, 0.841\}$  differ by less than 3%, except for  $c_0$  that corresponds to a transition between transmon states not hybridized with mode  $O$ . (b)  $p(n)$  cuts (also shown in a) at  $A = 0$  (blue),  $0.45$  (green),  $0.8$  (magenta) and  $1.3$  V (red) showing both measured data (dots with  $\pm 2\sigma$  error bars) and expected Poisson distributions (lines). Residual errors between data and fit are homogeneously distributed all over the dataset (not shown) and Gaussianly distributed with a standard deviation  $\sigma = 0.6\%$  and a shift of  $0.1\%$  (left inset). Right inset is the reconstruction of the Wigner function of a targeted state  $|\beta = -\sqrt{5} + i\sqrt{2}\rangle$  by tomography and maximum likelihood analysis (see text).

are calibrated in amplitude for  $n \in [0, 10]$ .

Because of many possible imperfections in the transfer or readout process of  $p(n)$ , such as different relaxation

times of  $|+n\rangle$  for different  $n$  during drive and/or readout, the  $p(n)$  measurement method is carefully calibrated as described now: A series of rectangular pulses with fixed frequency  $\nu_{\tilde{O}}$ , fixed  $0.3\ \mu\text{s}$  long duration, and increasing amplitudes  $A$  are used to generate a priori coherent states  $|\beta\rangle$  in  $\tilde{O}$ ; immediately after, a  $\pi$  pulse is applied on one of the  $+n$  transition, and the relative decrease  $s(n, A) = \Delta S_{21}(\nu_R, g)$  of the readout mode transmission is measured with a final pulse; this signal, averaged over 40000 sequences (separated by  $\sim 6T_O$  to let the field relax to its ground state) is measured for  $n \in [0, 10]$  and for 26 values of  $A$ . Then a model assuming that the coherent amplitude  $\beta = kA$  is proportional to the input amplitude  $A$  and that the raw signal  $s(n, A)$  reproduces the Poisson distribution  $p_\beta(n)$  of coherent states  $|\beta\rangle$  up to calibration coefficients  $c_n$  that depend only on  $n$ , is fitted to the whole data set. The fit  $s(n, A) = c_n p_{kA}(n)$ , shown in Fig. 4, yields the eleven parameters  $\{c_0, \dots, c_{10}\}$  as well as the filling rate  $k = 2.29\ \text{V}^{-1}$ . The residual error of the fit is homogeneously and Gaussianly distributed with a standard deviation of only  $0.6\%$ , which confirms the validity of the model.

The calibration coefficients  $c_n$  being known, the occupation probabilities  $p_\rho(n) = s(n, \rho)/c_n$  can now be measured to fully characterize any state  $\rho$  of the oscillator field using standard quantum field tomography [23] and maximum likelihood techniques [24]. As a demonstration, we target a coherent state  $|\beta = -\sqrt{5} + i\sqrt{2}\rangle$ , prepare it using a coherent rectangular pulse with proper amplitude and phase, and then measure it. This is done by recording the Fock state probabilities  $p(n, \gamma)$  for  $n \in [0, 7]$  and for 240 different complex displacements  $\gamma$  of  $|\beta\rangle$ , and then reconstructing the field density matrix  $\rho$  in a Hilbert space truncated to 18 photons, by maximizing the likelihood of the  $\{p(n, \gamma)\}$  dataset. The corresponding Wigner function is shown in the bottom inset of Fig. 4b. The fidelity  $\text{Tr}(\sqrt{\sqrt{\rho}}|\beta\rangle\langle\beta|\sqrt{\sqrt{\rho}})$  of the reconstructed  $\rho$  to the targeted state is of order 98% immediately after the calibration (the calibration has to be done every three days, typically).

### C. Non-linearities of the oscillator

We now check experimentally our claim of a very small Kerr effect for the 'ef-resonant' scheme. With the  $g_O = 7.45\ \text{MHz}$  and  $\alpha = -261\ \text{MHz}$  values determined spectroscopically, the Kerr non-linearity calculated for the three level transmon model of section I is  $K = -346\ \text{Hz}$  per photon. However, when diagonalizing numerically the Hamiltonian of the system including the fourth transmon energy level, the Kerr effect is found to be even smaller, to depend on  $n$ , and to cancel and reverse its sign at about 20 photons. Such an ultra-small Kerr effect would yield no sizable phase accumulation of the different Fock states over the cavity relaxation time  $T_O = 54\ \mu\text{s}$ . This makes it difficult to measure it dynamically, by recording either the trajectory of a field state in phase space as in

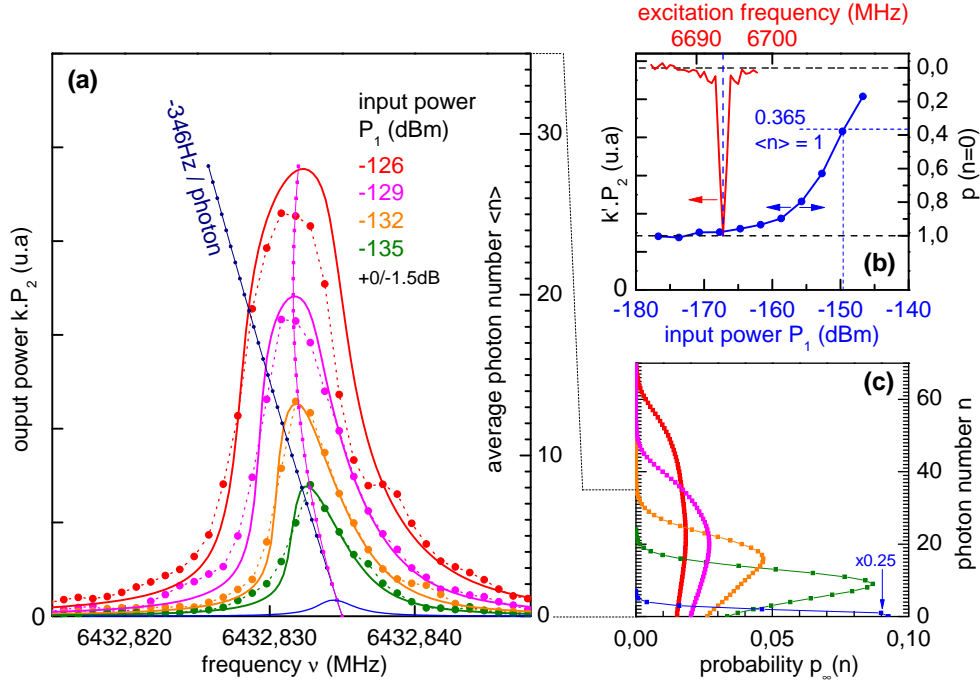


Figure 5. Steady state non-linearities of oscillator  $\tilde{O}$  in the 'ef-resonant' condition. (a) Transmitted power (in linear units) measured with the VNA (dots joined by dotted lines) for input powers  $P_1$  varying from -135 dBm to -126 dBm by steps of 3dB. Solid lines are the steady state average photon number  $\langle n \rangle$  in mode  $\tilde{O}$  simulated numerically (see text) for the same  $P_1$  values according to calibration, and for  $P_1 = -149.6$  dBm ( $\langle n \rangle = 1$ ) at resonance. The non-linearity in frequency calculated with four transmon levels (magenta line) is smaller than -346 Hz/photon Kerr constant (dark blue line). A large non-linearity in power is however observed (see text). (b) Calibration of  $P_1$  versus  $\langle n \rangle$ . Red: variation of the transmitted readout amplitude  $|P_2(\nu)|$  when keeping mode  $\tilde{O}$  in its ground state and detuning the qubit excitation frequency  $\nu$  of a  $\pi$  pulse away from the  $+0$  transition at  $\nu_{ge}$  (dashed vertical line). Blue: Same readout amplitude after the resonant qubit  $\pi$  pulse when filling  $\tilde{O}$  by a continuous tone with frequency  $\nu_{\tilde{O}}$  and variable input power  $P_1$ . The average photon number  $\langle n \rangle$  reaches 1 at  $P_1 = -149.6$  dBm (blue dashed lines - see text). (c) Simulated photon number distributions  $p_\infty(n)$  at the top of each simulated resonance of panel (a). The blue curve for  $\langle n \rangle = 1$  has been multiplied by 0.25 for clarity.

[14, 18], or the power dependence of the resonance line shape at short time as in the supplementary information of [14]. Consequently, we simply measure the steady-state transmitted power  $P_2(\nu)$  of mode  $\tilde{O}$  as a function of the excitation frequency  $\nu$  at several input powers  $P_1$ , using the VNA with a narrow enough measuring bandwidth of 1 kHz. The corresponding curves are shown in Fig. 5a (dots) in arbitrary units of the output power  $P_2$  (left scale).

Analyzing quantitatively the dataset requires a precise knowledge of the average photon number  $\langle n \rangle$  in the resonator as a function of  $\nu$  and  $P_1$ . In this aim, we perform the following additional in-situ calibration and data analysis. We first use the transmon to determine experimentally the input power  $P_{1,1} = -149.6$  dBm that populates the cavity with  $\langle n \rangle = 1$ , which corresponds to  $p_{\beta=1}(n=0) = 0.365$  (see Fig. 5b) assuming a coherent steady state  $\rho_1 = |\beta=1\rangle\langle\beta=1|$ . Then quantum simulations of the oscillator  $O$  coupled to the effective 4 level transmon are performed using the QuTiP Python toolbox [25], the already mentioned measured parameters, and the calibrated  $P_1$ . Solid lines in Fig. 5a show

the resonance lines  $\langle n \rangle(\nu)$  obtained with the steady state solver of QuTiP. By scaling vertically the experimental curves so that simulation and experiment match for  $P_1 = -135$  dBm, we obtain a fair agreement for all curves, leading to the following results: First the resonance lines display indeed a very small Kerr effect, with a shift towards lower frequency with increasing  $P_1$  significantly smaller than  $K$  (oblique dark blue line), and changing sign between  $\langle n \rangle = 15$  and 25, in good agreement with the calculated shift (magenta line).

A second and unanticipated effect is that although the non-linearity in frequency is small, a large non-linearity in input power is observed, with  $P_2$  and  $\langle n \rangle$  increasing by a factor of only 3 when  $P_1$  is increased by a factor 8 (see extreme curves in Fig. 5a). Simulating the time evolution of the system initialized in its ground state and driven coherently at  $\nu_{\tilde{O}}$  reveals the cause of this non-linearity in  $P_1$ : the small hybridization of the oscillator with the transmon (see Eq. 3) that has finite coherence times ( $T_1, T_2^*$ ), progressively induces Fock state dephasing. The increasing field perfectly coherent at the beginning of the dynamics slowly becomes incoherent when ap-

proaching the steady state, which reduces its amplitude. This is illustrated in Fig. 5c by the photon number distributions  $p_{P_1, t=\infty}(n)$  obtained from the steady state solver at the top of each resonance curve of panel a: although  $p_{P_1, t=\infty}(n)$  corresponds almost exactly to the Poisson distribution for  $\rho_1$  (which validates the calibration of  $P_1$  in the previous section), the other distributions for larger  $\langle n \rangle$  are less and less Poissonian. Large coherent states can nevertheless be obtained at times shorter than a few tens of  $T_2^*$ , as observed in the previous section for a duration of the coherent drive  $t \simeq T_2^*/8$ . Note that the transmon-induced cavity non-linearity in power observed and simulated here also exists in the dispersive regime, and is an effect that would deserve a theoretical evaluation.

#### IV. CONCLUSION

We have described a way to manipulate the quantum state of a harmonic oscillator by coupling it to an anharmonic multilevel system (MLS), without paying the price of a large Kerr non-linearity of the oscillator inherited from the MLS. We have demonstrated our 'ef-resonant' scheme using a 3D circuit-QED setup, in a new geome-

try involving a tunable transmon qubit partially inserted inside a single multimode superconducting cavity. Fock state manipulation was demonstrated by quantum state tomography of a coherent field in the cavity. The non-linearity was measured to be very small, provided the total field manipulation time is not much longer than the qubit coherence time. Our setup and coupling scheme provide a new platform for manipulating at will mesoscopic quantum fields inside a harmonic resonator, and producing non-classical states in various ways. In particular, the ef-resonant scheme would reduce the Kerr non-linearity of the promising platform proposed and developed [8, 26, 27] for encoding quantum information in Schrödinger cat states of the cavity field. We plan to use this scheme for demonstrating the quantum Zeno dynamics of the cavity field as proposed in [28].

#### ACKNOWLEDGMENT

We gratefully acknowledge discussions within the Qnantronics group, technical support from P. Orfila, P. Senat, J.C. Tack, D. Duet, and V. Padilla, as well as financial support from the European research contracts CCQED and ScaleQIT.

- 
- [1] S. Haroche and J.M. Raimond, *Eploring the Quantum* (Oxford University Press, Oxford, 2006)
  - [2] A. Blais *et al.*, PRA **69**, 062320 (2004).
  - [3] A. Wallraff *et al.*, Nature (London) **431**, 162 (2004).
  - [4] M. Brune *et al.*, Phys. Rev. Lett. **76**, 1800 (1996).
  - [5] C. K. Law and J. H. Eberly, Phys. Rev. Lett. **76**, 1055 (1996).
  - [6] M. Hofheinz *et al.*, Nature, **454**, 310 (2008).
  - [7] M. Hofheinz *et al.*, Nature, **459**, 546 (2009).
  - [8] Z. Leghtas *et al.*, Phys. Rev. A, **87**, 042315 (2013).
  - [9] D. I. Schuster *et al.*, Nature, **445**, 515 (2006).
  - [10] M. Brune *et al.*, Phys. Rev. Lett. **77**, 4887 (1996).
  - [11] R. W. Heeres *et al.*, Phys. Rev. Lett. **115**, 137002 (2015).
  - [12] S. Krastanov *et al.*, Phys. Rev. A **92**, 040303(R) (2015).
  - [13] S. Deléglise *et al.*, Nature, **455**, 510 (2008).
  - [14] G. Kirchmair *et al.*, Nature, **495**, 205 (2013).
  - [15] J. Koch *et al.*, Phys. Rev. A, **76**, 42319 (2007).
  - [16] J. Bourassa, F. Beaudoin, JM. Gambetta, and A. Blais, Phys. Rev. A **86**, 013814 (2012).
  - [17] S. E. Nigg *et al.*, Phys. Rev. Lett, **108**, 240502 (2012).
  - [18] Y. Yin *et al.*, Phys. Rev. A, **85**, 23826 (2012).
  - [19] B. Yurke and D. Stoler, Phys. Rev. Lett., **57**, 1 (1986).
  - [20] H. Paik *et al.*, Phys. Rev. Lett, **107**, 240501 (2011).
  - [21] D. Ristè *et al.*, Nature Comm., **4**, 1913 (2013).
  - [22] X. Zhou *et al.*, Phys. Rev. B, **89**, 214517 (2014).
  - [23] M.G.A Paris and J. Rehacek. Quantum State Estimation. Springer, 2004.
  - [24] Z. Hradil, J. Rehacek, J. Fiurasek, and M. Jezek, Maximum-likelihood methods in quantum mechanics, Lect. Notes Phys. **649**, 59 (2004).
  - [25] J. R. Johansson, P. D. Nation, and F. Nori, Computer Physics Communications **183**, 1760 (2012).
  - [26] B. Vlastakis *et al.*, Science, **342**, 6158 (2013).
  - [27] C. Wang *et al.*, Science, **352**, 6289 (2016).
  - [28] J.M. Raimond *et al.*, Phys. Rev. A, **86**, 32120 (2012).